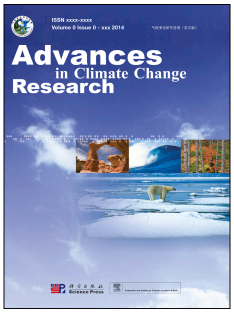

Declining snow depth in northwest Central Asia driven by atmospheric dynamics and thermodynamic warming

Meng-Yuan YAO, Hao-Su TANG, Gang HUANG

PII: S1674-9278(26)00083-3

DOI: https://doi.org/10.1016/j.accre.2026.04.008

Reference: ACCRE 759

To appear in: *Advances in Climate Change Research*

Received Date: 2 November 2025

Revised Date: 25 January 2026

Accepted Date: 16 April 2026

Please cite this article as: Meng-Yuan, Y., Hao-Su, T., HUANG, G., Declining snow depth in northwest Central Asia driven by atmospheric dynamics and thermodynamic warming, *Advances in Climate Change Research*, https://doi.org/10.1016/j.accre.2026.04.008.

Declining snow depth in northwest Central Asia driven by atmospheric dynamics and thermodynamic warming

Meng-Yuan YAO[1,2], Hao-Su TANG[3*], Gang HUANG[1,2**]

[1]*Sate Key Laboratory of Earth System Numerical Modeling and Application, Institute of Atmospheric Physics, Chinese Academy of Sciences, Beijing 100029, China*

[2]*University of Chinese Academy of Sciences, Beijing 100049, China*

[3]*School of Geography and Planning, University of Sheffield, Sheffield S10 2TN, UK*

* Corresponding author. haosu.tang@sheffield.ac.uk (TANG H.-S.) School of Geography and Planning, University of Sheffield, Sheffield S10 2TN, UK

** Corresponding author. hg@mail.iap.ac.cn (HUANG G.)

Sate Key Laboratory of Earth System Numerical Modeling and Application, Institute of Atmospheric Physics, Chinese Academy of Sciences, Beijing 100029, China

Declining snow depth in northwest Central Asia driven by atmospheric dynamics and thermodynamic warming

Meng-Yuan YAO[1,2], Hao-Su TANG[3*], Gang HUANG[1,2**]

[1]*Sate Key Laboratory of Earth System Numerical Modeling and Application, Institute of Atmospheric Physics, Chinese Academy of Sciences, Beijing 100029, China*

[2]*University of Chinese Academy of Sciences, Beijing 100049, China*

[3]*School of Geography and Planning, University of Sheffield, Sheffield S10 2TN, UK*

* Corresponding author. haosu.tang@sheffield.ac.uk (TANG H.-S.) School of Geography and Planning, University of Sheffield, Sheffield S10 2TN, UK

** Corresponding author. hg@mail.iap.ac.cn (HUANG G.)

Sate Key Laboratory of Earth System Numerical Modeling and Application, Institute of Atmospheric Physics, Chinese Academy of Sciences, Beijing 100029, China

Abstract

The relative roles of atmospheric circulation and thermodynamic warming in driving the rapid decline of winter snow depth (SD) in northwest Central Asia (CA) remain poorly quantified, despite their opposing influences on regional snow variability. Here, based on observational datasets with large-ensemble climate model simulations, dynamical adjustment reveals that circulation-driven processes account for SD accumulation of 0.22 mm per year ($p < 0.1$) during 1979–2024, whereas thermodynamically driven warming overwhelms this effect, producing an SD shallowing of −1.00 mm per year ($p < 0.1$). Among circulation influences, externally forced sea surface temperature (SST) anomalies explain 82% of the dynamical SD changes, with the remainder dominantly governed by internally generated SST anomalies. Both eastern Pacific cooling and North Atlantic warming induce northerly and easterly anomalies over northwest CA, enhancing cold advection and favoring snow accumulation. Moreover, winter SD exhibits a predictive influence on subsequent spring climate. These findings underscore the combined influence of dynamic and thermodynamic processes in shaping SD decline in northwest CA, providing insights for water resource management and regional climate adaptation.

Keywords: Snow depth; Central Asia; Dynamical adjustment; Atmospheric circulation

1. *Introduction*

Seasonal snow cover serves as a vital source of freshwater, whose snowmelt exerts profound impacts on the surface energy balance, hydrological cycle, and ecological processes, especially in arid and semi-arid areas (Chevallier et al., 2014; Dietz et al., 2014). Central Asia (CA), encompassing Uzbekistan, Tajikistan, Turkmenistan, Kyrgyzstan, and Kazakhstan, is the largest arid and semi-arid region globally, where snow water equivalent contributes more than 50% of the total runoff in major river basins such as the Amu Darya and Syr Darya (Hoelzle et al., 2017; Yao et al., 2019). Ongoing warming is shifting precipitation from snow to rain, ultimately leading to increased water loss during winter and early spring (Barnett et al., 2005; Li et al., 2020a). Such changes pose substantial risks to water resources and agriculture in CA. For example, in Uzbekistan, rice production in 2001 decreased by more than 50% compared to 2000 due to insufficient rainfall and severe water shortages for irrigation (FAO, 2001). Therefore, a comprehensive investigation of winter snow cover dynamics in CA is essential for assessing hydroclimatic risks and informing ecological conservation, water resource management, and sustainable economic development (Koster et al., 2010; Yao et al., 2021).

In recent decades, snow cover in CA has undergone substantial but spatially heterogeneous changes. Snow depth (SD) has declined in the west–central region but increased in the northeast CA, accompanied by a shift in snowfall phase, including a post-1990s decline in snowfall fraction and an increase in extreme snowfall events (Li et al., 2019; Li et al., 2020a; Lin et al., 2024). Elevation-dependent responses are also evident, with reduced snow cover duration at high elevations (>3000 m) due to earlier melt, contrasted by advancing snow onset atmid-elevations (Dietz et al., 2014; Zhou et al., 2017). Such SD variability reflects the combined influence of internal climate variability and external forcing, mediated by atmospheric circulation, which modulates climatic factors such as surface temperatures, moisture transport, and wind fields (Koster et al., 2010; Chen et al., 2023; Ma et al., 2025). As a region particularly sensitive to climate change, persistent warming is anticipated a phase transition from snowfall to rainfall and advancing snowmelt in CA (Li et al., 2020a), deteriorating water scarcity during the warm season (Chen et al., 2016; Jiang et al., 2025). Nevertheless, regional warming and wetting could also favor more intense snowfall events due to enhanced atmospheric instability (Li et al., 2019; Wang et al., 2020).

Beyond local climate influences, sea surface temperature (SST) variability provides a vital source of teleconnection forcing. Tropical Pacific warming can trigger eastward-propagating wave trains, generating anomalous cyclones over CA, enhancing moisture convergence, and ultimately increasing snowfall frequency (Chen et al., 2022; Chen et al., 2023). Simultaneously, interactions between the North

Atlantic Oscillation and tripole North Atlantic SST may amplify these wave trains (Chen et al., 2023; Man et al., 2025). Besides, previous studies have also shown that Rossby wave train along the westerly jet stream induced by Atlantic SST anomalies could influence Eurasian atmospheric circulation, further contributing to the frequency of extreme precipitation events (Han et al., 2018; Zhang et al., 2020).

On the other hand, anthropogenic impacts on Eurasian snowfall variability are increasingly discernible, typically manifesting as a decline in snowfall events (Gottlieb et al., 2024). During the historical period, anthropogenic forcings have largely explained reductions in snow days and light snowfall days across Eurasia, with greenhouse gas emissions playing a dominant role (Lin et al., 2024). Additionally, anthropogenic warming not only delays snow onset and advances snowmelt but also enhances the frequency of intense snowfall events due to increased atmospheric moisture availability (Chen et al., 2020). Furthermore, the deposition of black carbon exacerbates snowmelt by reducing surface albedo and enhancing radiative forcing (Schmale et al., 2017; Zhang et al., 2019).

Despite these advances, the mechanisms governing the long-term decline of SD in CA remain unresolved, particularly the extent to which atmospheric circulation changes versus thermodynamic warming control regional SD trends. Here we address this gap by disentangling the contributions of atmospheric dynamics, externally forced responses, and internal climate variability to recent SD changes in CA. We further identify the key oceanic drivers underpinning these variations, with a focus on coupled Pacific–Atlantic SST anomalies and their influence on regional circulation. By quantifying the respective roles of dynamical and thermodynamical processes, our results provide a process-based framework for understanding SD decline in CA. Beyond attribution, this study highlights the potential of winter SD as an indicator of subsequent hydroclimatic conditions, offering new insights into seasonal predictability and water resource risk in a warming climate.

2. Data and methods

2.1 Data

We primarily use monthly SD from the Fifth-generation European Centre for Medium-Range Weather Forecasts (ECMWF) atmospheric reanalysis (ERA5) at a horizontal resolution of 0.25° × 0.25° (Hersbach et al., 2020). The reliability of ERA5 SD over CA has been evaluated through comparison with station-based observations from the Global Historical Climatology Network daily dataset (GHCNd) (Menne et al., 2012). Additionally, three additional monthly SD datasets are also analyzed, including the Japanese 55-year Reanalysis version 3Q (JRA-3Q; 1.25° × 1.25°) (Kosaka et al., 2024), the Modern-Era Retrospective Analysis for Research and Applications, version 2 (MERRA-2; 0.625° × 0.625°) (Gelaro et al., 2017), and the Global Land Data Assimilation System (GLDAS; 0.25° × 0.25°) (Rodell et al., 2004). Observed monthly precipitation and surface air temperature (T2m) are obtained from the Climatic Research Unit dataset, version 4.09 (CRU TS4.09; 1.25° × 1.25°) (Harris et al., 2020), while observed monthly SST is sourced from the Hadley Centre Sea Ice and Sea Surface Temperature dataset (HadISST; 1° × 1°) (Rayner et al., 2003). In parallel, a wide range of atmospheric variables from ERA5 are employed to diagnose the associated physical mechanisms, including three-dimensional atmospheric temperature, sea-level pressure (SLP), dew point temperature, geopotential height, and zonal and meridional winds (Hersbach et al., 2020).

Apart from the observational and reanalysis datasets, two large-ensemble climate model datasets are employed. Both provide historical simulations for 1850–2014 and future projections under the Shared Socioeconomic Pathway 5-8.5 (SSP5-8.5) scenario for 2015–2100. The two selected models—CanESM5 and MIROC6—span the high- and low-sensitivity ends of equilibrium climate sensitivity (ECS), respectively, which quantifies the global mean temperature response to a doubling of atmospheric CO_2. Both models provide 50 ensemble members (Swart et al., 2019; Tatebe et al., 2019), enabling a robust characterization of forced and internally generated climate components. Large-ensemble model means are widely recognized as an effective approach for isolating externally forced climate signals (Deser et al., 2012; Dai et al., 2015; Wu et al., 2021). Compared to limited ensemble members, the ensemble mean of a large ensemble model effectively cancels out internal variability, such as nonlinear interactions within the atmosphere, ocean, and land surface, thereby yielding a cleaner estimate of the forced response. This separation allows internally generated variability to be diagnosed from the residual between observations and the externally forced signal (Deser et al., 2012; Dai et al., 2015; Qin et al., 2020). All model simulations are bilinearly interpolated onto a uniform 1° × 1° horizontal grid before analysis.

Boreal winter is defined as December of the preceding year, January, and February. An 11-year running mean is applied to isolate low-frequency variability and suppress year-to-year fluctuations. The primary focus of this study is SD evolution during the present-day period (1979–2024), while the mechanisms governing SD-related interdecadal changes are examined over an extended period (1941–2024) to enhance the robustness of the physical interpretation. Considering that models' historical simulations terminate in 2014, the ensemble mean is extended to 2024 by appending the SSP5-8.5 future projection.

2.2 Dynamical adjustment

The dynamical adjustment procedure is applied to decompose observed SD into dynamical and thermodynamic components, following a framework that integrates observations and model simulations to elucidate inter-model and externally forced signals (Deser et al., 2016; Li et al., 2024). This method is based on the premise that large-scale atmospheric circulation exerts dominant control over local climate variability, whereas residuals unexplained by circulation reflect thermodynamic contributions and other unexplained circulation responses, of which term is dominated by anthropogenic warming with greenhouse gas and aerosol forcings. Here, mid-tropospheric circulation is represented by the 500-hPa eddy geopotential height (Z500), which isolates regional circulation anomalies from the zonal-mean background state and serves as a robust proxy for dynamical changes in the mid-troposphere. For each target year *t*, a pool of Z500 patterns is constructed by excluding year *t* and randomly subsampling 30 Z500 fields from the remaining years within the corresponding climate period (1979–2024 for the present climate and 2054–2099 for the future projection). An ordinary least squares regression model is then trained using the subsampled Z500 patterns to reconstruct the Z500 field for the target year *t*. The derived regression coefficients are subsequently used to reconstruct the corresponding circulation-induced SD field. To reduce sampling uncertainty and mitigate overfitting, this subsampling and reconstruction process is repeated 100 times. As a result, the dynamical component of the SD field is obtained by averaging the results from these 100 reconstructions, yielding the best estimate of the dynamical-induced SD field. The thermodynamic component is then derived by subtracting the dynamical-induced SD from the observed total SD. A summary of this process is outlined in the flowchart in Fig. A1.

Furthermore, given that both internally generated and externally forced SST variability can modulate atmospheric circulation patterns, the dynamical contribution to SD (C_{Dyn}) can be decomposed into three components:

$$C_{\mathrm{Dyn}} = C_{\mathrm{INTS}} + C_{\mathrm{FORS}} + C_{\mathrm{IAC}} \quad (1)$$

where C_{INTS} and C_{FORS} represent the teleconnection related SD, which could be driven by internal variability and external forces of SST modes, respectively. C_{IAC} represents the residual term related to local atmospheric circulation.

2.3 SST-based attribution of interdecadal dynamical SD variability

Given the documented influence of interdecadal SST modes in the equatorial Pacific and the North Atlantic on CA (Chen et al., 2023; Yao et al., 2024b), two SST indices are defined to quantify their respective contributions to the dynamically induced SD trends. The Interdecadal Pacific Oscillation (IPO) index is defined as the winter-mean SST anomaly difference between the central equatorial Pacific (10°S–10°N, 170°E–90°W) and the mean of the Northwest and Southwest Pacific regions (25°N–45°N, 140°E–145°W and 50°S–15°S, 150°E–160°W) (Liu et al., 2024; Yao et al., 2025). The Atlantic Multidecadal Variability (AMV) index is defined as detrended winter-mean SST anomalies averaged over the North Atlantic basin (0°–65°N, 80°W–0°) (Yao et al., 2025). Additionally, the robustness of the IPO and AMV definitions is assessed using alternative spatial domains, running-mean windows (9- and 11-year), and detrending strategies, including linear detrending and removal of the global-mean SST signal for AMV. The results demonstrate that the 11-year running averaged IPO and AMV indices are highly robust, with strong correlations (≥0.74; $p < 0.1$) among alternative definitions over 1941–2024 (Table A1).

To disentangle internally generated and externally forced SST-related contributions to interdecadal SD variability, maximum covariance analysis (MCA) is applied to the covariance matrix between the observed dynamically induced SD field and global SST anomalies (50°S–60°N) over the extended period 1941–2024. The SST field used in the MCA can be either the observed SST anomalies or their internally generated and externally forced components derived from large-ensemble climate model simulations. The leading MCA mode (MCA1) of SST and its explained covariance fraction are robust across different SST domains (60°S–60°N and 80°S–80°N). Based on the MCA results, the principal component (PC1) of dynamically induced SD is obtained for each SST configuration (observed, internally generated, and externally forced). The IPO and AMV indices derived consistently from the corresponding SST fields are then jointly regressed onto the SD PC1 over 1941–2024. This regression framework allows the interdecadal SD variability associated with IPO and AMV to be reconstructed separately for internally generated and externally forced SST components. Furthermore, the contributions of IPO and AMV to the dynamically induced SD trend during the present period (1979–2024) are quantified by combining the IPO- and AMV-related trends in the SD PC1 and the explained covariance fraction of MCA1, and subsequently scaling by the corresponding SD PC1 trend. The internally generated and externally forced contributions are expressed as:

$$\frac{\partial C_{\mathrm{INTS}}}{\partial t} = s_{\mathrm{INTS\ IPO}} \frac{\partial \mathrm{IPO}_{\mathrm{INTS}}}{\partial t} + s_{\mathrm{INTS\ AMV}} \frac{\partial \mathrm{AMV}_{\mathrm{INTS}}}{\partial t} \tag{2}$$

$$\frac{\partial C_{\mathrm{FORS}}}{\partial t} = s_{\mathrm{FORS\ IPO}} \frac{\partial \mathrm{IPO}_{\mathrm{FORS}}}{\partial t} + s_{\mathrm{FORS\ AMV}} \frac{\partial \mathrm{AMV}_{\mathrm{FORS}}}{\partial t} \tag{3}$$

Where s denotes the regression coefficients obtained by projecting the internally generated or externally forced normalized IPO and AMV indices onto the corresponding SD PC1 over 1941–2024. $\frac{\partial}{\partial t}$ represents linear trends evaluated over the present period (1979–2024).

2.4 K index and wave-activity fluxes

The *K* index is a measure of atmospheric stability, which quantifies the extent to which an air parcel returns to or deviates from its equilibrium position after being vertically disturbed (Wang et al., 2020).

The index represents the temperature lapse rate, middle-level moisture conditions, and the level of saturation in the lower troposphere. A higher K index indicates a more unstable atmospheric stratification, which favors the thermodynamic development of intense convective turbulence.

Additionally, horizontal wave-activity fluxes are also used to diagnose the propagation and dynamical influence of quasi-stationary atmospheric waves (Takaya et al., 2001).

2.5 Effective degrees of freedom

To account for the potential autocorrelation associated with interdecadal variability, we adjust the nominal sample size when assessing statistical significance. Because adjacent data points in climate time series are not strictly independent, ignoring serial correlation can lead to an overestimation of the effective degrees of freedom and inflated significance levels. The effective degrees of freedom, consistent with Pyper et al. (1998), explicitly account for the influence of multi-order serial correlation in both variables, which is particularly relevant for low-frequency climate signals such as interdecadal variability.

3. Results

3.1 Dynamical and thermodynamical contribution to SD trends

During the common period of the multi-source datasets (1981–2014), winter SD trends across CA exhibit a pronounced quasi-dipole spatial pattern, with robust SD declines over northwestern CA consistently identified across multiple gridded reanalysis products, and weaker and less consistent SD increases over eastern and southern CA (Fig. A2). This spatial contrast is further supported by trends derived from quality-controlled GHCNd station observations (Fig. A2), based on stations with at least 40% of valid winter records during 1981–2014. The threshold is adopted to balance station availability and data continuity in this data-sparse region, allowing for a reliable assessment of regional-scale SD trends identified from gridded products. Meanwhile, sensitivity tests using 50% and 60% thresholds yield similar spatial patterns. Beyond data consistency, SD changes over northwest CA are of particular climatic and hydrological significance, as this region serves as a major snow accumulation zone feeding the headwaters of the Amu Darya, Syr Darya, and Ural River systems. Given both the robustness of the observed SD decline and its disproportionate importance for regional water resources, we therefore focus subsequent analyses on northwest CA (45°–70°E, 46°–58°N; yellow boxes in Fig. A2).

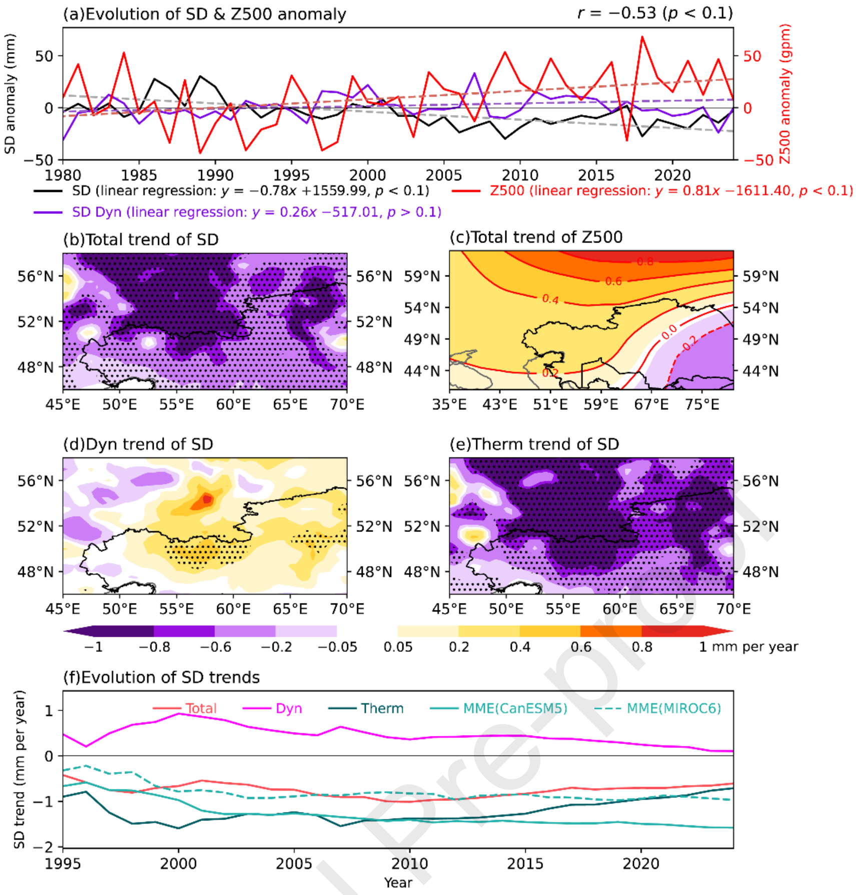

Fig. 1. (a) Time series of areal averaged SD and Z500 anomalies over northwest Central Asia (45°–70°E, 46°–58°N) (The correlation coefficient between SD and Z500 is shown, and Z500 is defined as the deviation from the zonal mean at each latitude, isolating regional circulation anomalies from the large-scale background), trends of (b) total SD and (c) Z500, (d) dynamical and (e) thermodynamical SD trends in winter during 1979–2024 (Stippled areas represent the significance exceeding 90% confidence level), and (f) time series of total, dynamical and thermodynamical SD trends in observation and MME from CanESM5 and MIROC6 in different periods starting from 1979 (The *x*-axis represents the final year of the calculated trend period).

Winter SD anomalies relative to the climatological mean (1979–2010) reveal a spatially homogeneous decline across northwest CA in the present period of 1979–2024. The area-averaged decline rate is −0.78 mm per year based on ERA5, above sixfold the Northern Hemisphere average of −0.12 mm per year (Fig. 1a, b). Meanwhile, the mid-tropospheric circulation over northwest CA undergoes a marked strengthening of Z500, with a significant increasing trend of 0.81 gpm per year, characterized by high-pressure anomalies over northern and western CA and low-pressure anomalies in the southeast (Fig. 1a, c), enhancing northerly and easterly anomalies over northwest CA. This circulation configuration favors southward intrusions of cold continental air, thereby creating dynamical conditions favorable for snow accumulation. Therefore, Z500 is selected as the primary circulation proxy for the dynamical adjustment analysis over northwest CA, allowing for the separation of atmospheric circulation-driven (dynamic) contributions from residual variability that cannot be explained by circulation anomalies and primarily attributed to thermodynamic processes associated with background warming.

The dynamical-driven SD trends based on Z500 exhibit an overall increasing, with an area-averaged rate of 0.22 mm per year, characterized by significant SD increases ($p < 0.1$) over central and eastern northwest CA and weak SD shallow over the northwest corner (Fig. 1d). A broadly consistent spatial pattern is also reproduced when the dynamical adjustment is performed using SLP as the circulation proxy (Fig. A3), although the magnitude is relatively weaker. This discrepancy likely reflects the stronger susceptibility of SLP to near-surface boundary layer processes compared to mid-tropospheric circulation represented by Z500. The dynamically driven SD trends over northwest CA are insensitive to the choice of analysis period within 1979–2024, remaining persistently positive since 1995 despite pronounced interannual variability (Fig. 1f). This indicates that circulation-induced processes act to partly offset the observed SD decline during the present period.

After isolating the dynamical influence, the spatial pattern of residual thermodynamical-induced SD trends closely resembles the observed spatial pattern, exhibiting a widespread SD decrease across northwest CA (Fig. 1d). The robustness of the dynamical adjustment is further supported by the consistency between results derived from Z500 and SLP (Fig. A3). Additionally, the anthropogenically forced SD decline is further corroborated by the multi-member ensemble mean (MME) of the high- and low-ECS climate models CanESM5 and MIROC6, which simulate area-averaged SD decline rates of −1.60 and −0.77 mm per year (both $p < 0.1$), respectively, over northwest CA during the present period (Figs. 1–2). Together, these findings confirm that the net observed decrease is dominated by anthropogenic warming processes governed by greenhouse gas and aerosol forcings, while atmospheric circulation changes have partially offset for thermodynamically driven SD decline during 1979–2024.

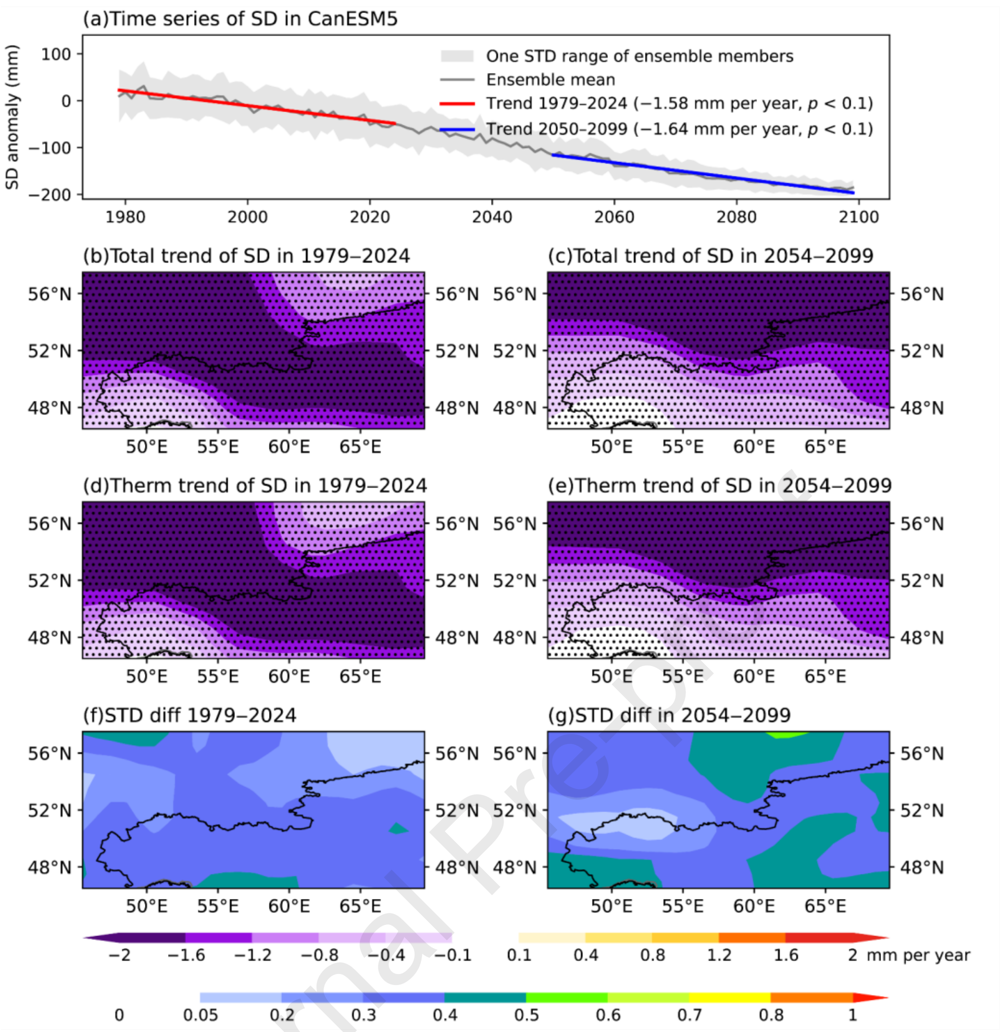

Fig. 2. (a) Time series of area-averaged SD anomalies relative to the 1979–2010 climatology over northwest CA (45°–70°E, 46–58°N) simulated by CanESM5 under the historical and SSP5-8.5 scenarios, (b–c) spatial patterns of total SD trends during 1979–2024 and 2054–2099, respectively (Stippled areas represent the significance exceeding 90% confidence level), (d–e) same as (b–c), but for thermodynamically induced SD trends, and (f–g) relative differences in one standard deviation of SD trends before and after dynamical adjustment, expressed as $(\mathrm{STD}_{\mathrm{before}} - \mathrm{STD}_{\mathrm{after}})/\mathrm{STD}_{\mathrm{before}}$.

Beyond the successful application of the Z500-based dynamical adjustment to present-day observations, we further apply the same framework to historical simulations and future projections from the CanESM5 and MIROC6 large ensembles under the SSP5-8.5 scenario. In both models, total SD persists to shallow from the present period toward the end of the 21st century, with a pronounced acceleration of the decline to −1.64 mm per year ($p < 0.1$) in CanESM5 and −1.41 mm per year ($p < 0.1$) in MIROC6 during 2054–2099 (Fig. 2a). For both the present and late-century periods, CanESM5 exhibits a stronger SD decline than MIROC6, consistent with its higher equilibrium climate sensitivity and associated stronger warming response (Zelinka et al., 2020). Following dynamical adjustment, the residual thermodynamic component of SD shows a spatial pattern highly consistent with the original simulated SD trends, with spatial correlation coefficients exceeding 0.90 in both models (Fig. 2; Fig. A4). In contrast, the dynamically driven component exhibits a near-zero spatial mean and can be effectively neglected, which should be interpreted as noise contributing to simulation uncertainty rather than as a physically meaningful circulation response (Deser et al., 2016). This distinction fundamentally differs from the observational dynamical component, which represents real-world atmospheric circulation changes. Consistent with this interpretation, the inter-member spread of SD trends—quantified by one standard deviation (STD Fig. 2a)—is substantially constrained after dynamical adjustment, yielding at least a 30% reduction in areal averaged inter-member uncertainty in both CanESM5 and MIROC6 relative to the unadjusted simulations (Fig. 2f, g; Fig. A4f, g). These results demonstrate the effectiveness of dynamical adjustment in isolating externally forced driven SD changes and in constraining model uncertainty, providing a robust basis for attributing the projected SD decline to anthropogenic warming.

3.2 Physical mechanisms for SD decline

Beyond local circulation processes, understanding the key dynamical teleconnection pathways through which circulation variability mitigates SD shallowing is essential. To identify the dominant large-scale drivers of dynamically induced SD variability, the MCA is applied between the observed dynamically driven SD component and detrended interdecadal SST anomalies, which play an important role in exciting planetary-scale wave trains that propagate into CA (Jiang et al., 2021; Chen et al., 2023). Both fields are smoothed using an 11-year running mean and analyzed over the extended period 1941–2024 to avoid spurious linkages arising from short records and to robustly isolate interdecadal signals.

The leading MCA mode (MCA1) explains 32% of the linkage between dynamically driven SD and SST variability. The SD MCA1 pattern is characterized by widespread positive anomalies across northwest CA, except for negative signals over the western and northeastern corners (Fig. 3a). This pattern is accompanied by a distinctive SST configuration featuring homogeneous warm anomalies over the North Atlantic and the northwest and southwest Pacific, and central equatorial Pacific cooling (Fig. 3b). The associated SST PC1 exhibits a strong positive correlation with the AMV of 0.91 and a strong negative correlation with the IPO of −0.81, both statistically significant based on effective degrees of freedom ($p < 0.1$). Importantly, the IPO and AMV indices are mutually independent ($p > 0.1$), indicating that their combined influence represents a linear superposition of two distinct modes of low-frequency ocean variability. The combined influence of a positive AMV and negative IPO phase is further confirmed by regressions of SST onto dynamically driven SD PC1 (Fig. 3c, f), demonstrating that large-scale dynamical SD accumulation over northwest CA is closely tied to these two interdecadal SST modes. This relationship can be well reconstructed by a linear combination of −0.18IPO + 0.17AMV over 1941–

2024, yielding an exceptionally high goodness of fit ($R^2 = 0.93$). In parallel, during the present period, the PC1 of dynamically driven SD exhibits a significant positive trend ($p < 0.1$).

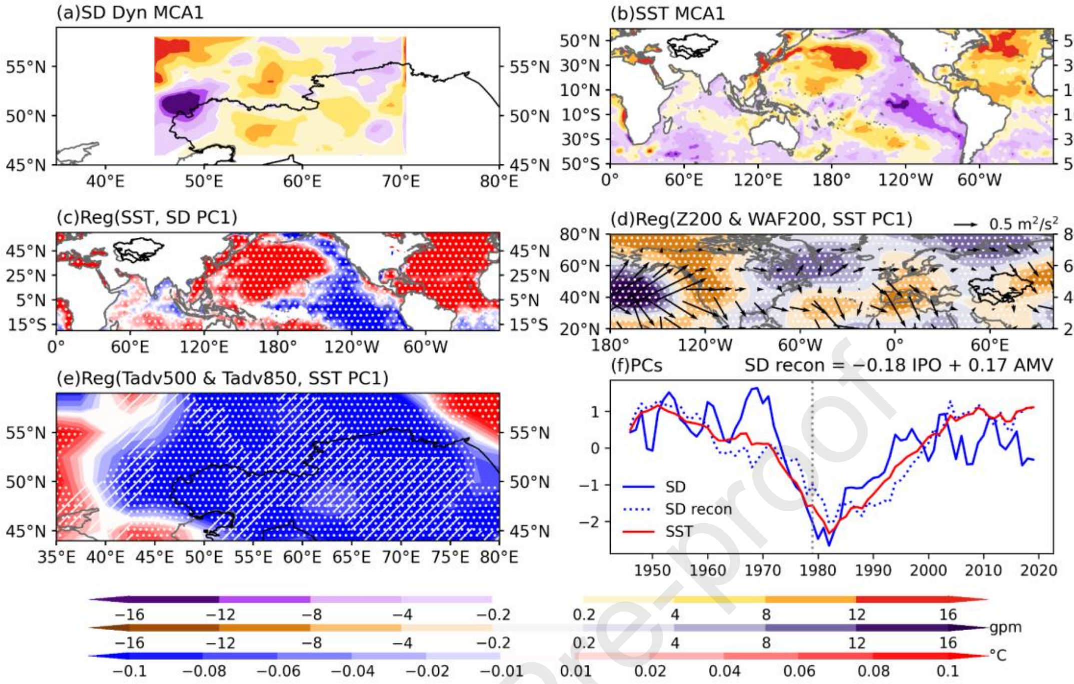

Fig. 3. (a–b) Leading maximum covariance analysis (MCA1) spatial patterns between dynamically induced SD and detrended global SST anomalies, (c) regression of SST anomalies onto the first principal component (PC1) of dynamically induced SD (Stippled areas indicate regression coefficients significant at the 90% confidence level), (d) same as (c), but for regressions of 200-hPa eddy geopotential height (shading) and wave activity flux (vector), (e) same as (c), but for 500-hPa (shading) and 850-hPa (hatched) horizontal temperature advection ($-\vec{V} \cdot \nabla T$; only significantly negative values with $p < 0.1$ are shown) onto the SST PC1, and (f) normalized PC1 time series of dynamically induced SD and SST.

To elucidate the underlying dynamical pathways, 200-hPa eddy geopotential height and wave activity flux is regressed onto the SST PC1. The resulting pattern reveals a quasi-stationary Rossby wave train originating from the equatorial eastern Pacific propagates eastward across the North Atlantic, ultimately inducing positive pressure anomalies over western Siberia and anomalous low pressure over central and eastern CA (Fig. 3d). Previous studies have found that warm SST anomalies in the North Atlantic may reinforce the eastward-propagating wave train induced by cooling SST anomalies in the tropical eastern Pacific (Chen et al., 2023; Man et al., 2025). This upper-level circulation configuration favors enhanced northerly and easterly anomalies over CA, facilitating southward cold-air intrusions into northwest CA. Consistent with this, regressions of lower- and mid-tropospheric air temperature advection onto the SST PC1 show pronounced cold advection over most of northwest CA, with weak warm advection confined to the western and northeastern corners (Fig. 3e), closely resembling the spatial pattern of the dynamical SD MCA1 pattern. These results demonstrate that circulation anomalies associated with a negative IPO and positive AMV phase enhance cold-air transport and dynamically favor SD accumulation over northwest CA.

An unstable atmospheric environment and reduced surface net shortwave radiation can potentially intensify snowfall events and SD variability (Wu et al., 2014; Wang et al., 2020; Sun et al., 2021). To assess their impact on SD changes, the regressions of K index and surface net shortwave radiation flux against SD are examined (Fig. A5). K index exhibits a significant positive correlation ($p < 0.1$) with SD over most of northwest CA though the relationship over northern northwest CA is weaker, reflecting coordinated contributions of dynamical and thermodynamical processes (Fig. A5a). Dynamically, an increased K index, particularly over central and eastern northwest CA, is associated with a steeper vertical temperature lapse rate in the troposphere. That arises from wider circulation-induced cold advection at mid-levels relative to the lower troposphere, modulated by easterly and northerly anomalies (Figs. 3e and A5c). In contrast, from a thermodynamical perspective, positive K index anomalies suggest increased atmospheric moisture content under global warming (Held et al., 2006; Oki et al., 2006), characterized by higher low- and mid-tropospheric humidity and a deeper moist layer (Fig. A5e). This thermodynamic enhancement further promotes snow accumulation by increasing precipitation efficiency. Such synergistic contributions of these dynamical and thermodynamical effects can promote intense snowfall events, including convective snowstorms, thereby favoring SD accumulation. Additionally, surface net shortwave radiation exhibits thermodynamically dominated feedback with SD (Fig. A5b). Reduced SD leads to lower surface albedo, increasing absorbed shortwave radiation and accelerating surface warming and snowmelt. This positive snow–radiation feedback amplifies SD loss, while the dynamically induced component remains weak and spatially incoherent (Fig. A5d, f). As a result, the SD–shortwave radiation relationship is primarily governed by thermodynamic processes, effectively overwhelming any minor dynamical influence.

3.3 Relative contributions responsible for dynamical SD trends

The observed warming in the North Atlantic and cooling in the equatorial eastern Pacific jointly influence SD in northwest CA, reflecting a combined teleconnection influence excited by internal variability and external forcing linked to global warming. This underscores the need for further investigation to precisely quantify the relative contributions of these factors. The MME of SST anomalies, which largely cancels out stochastic internal-member noise, provides an effective representation of climate changes driven by external forced SST signal dominated by greenhouse gas and aerosol forcing. Meanwhile, the residual obtained by subtracting the MME from observations is interpreted as internal SST variability. MCA is applied respectively between observed dynamical SD and i) externally forced and ii) internally generated global interdecadal detrended SST anomalies in 1941–2024. In both cases, MCA1 exhibits a dynamical SD pattern that closely resembles that obtained using observed total SST, indicating a robust linkage between SD dynamics and large-scale SST variability across different SST components (Figs. 3a and 4a, b). Specifically, the externally forced SST MCA1 pattern is characterized by near-global ocean warming, except for weak cooling over the southeastern Pacific. This mode explains 72% of the linkage between externally forced SST and dynamical SD, and the associated SST PC1 is significantly negatively and positively (both $p < 0.1$) correlated with the externally forced IPO and AMV based on effective degrees of freedom of 9 and 11, respectively, and can be well reconstructed as −0.10IPO + 0.18AMV. On the other hand, the internally generated SST MCA1 pattern features pronounced cooling in the central-eastern equatorial Pacific and a North Atlantic tripole pattern, with midlatitude cooling and warming in the high latitudes and tropics. This mode explains 40% of the covariance between internal SST variability and dynamical SD. Notably, the internal SST PC1 shows no significant interdecadal correlation ($p > 0.1$) with the internally generated IPO, but exhibits a significant negative correlation with the internally generated AMV ($p < 0.1$). Nevertheless, to ensure robustness and to avoid overfitting the dynamical SD PC1 to a single SST mode, we consistently retain both IPO and AMV in the reconstruction framework, yielding a combined relationship of −0.01IPO − 0.21AMV.

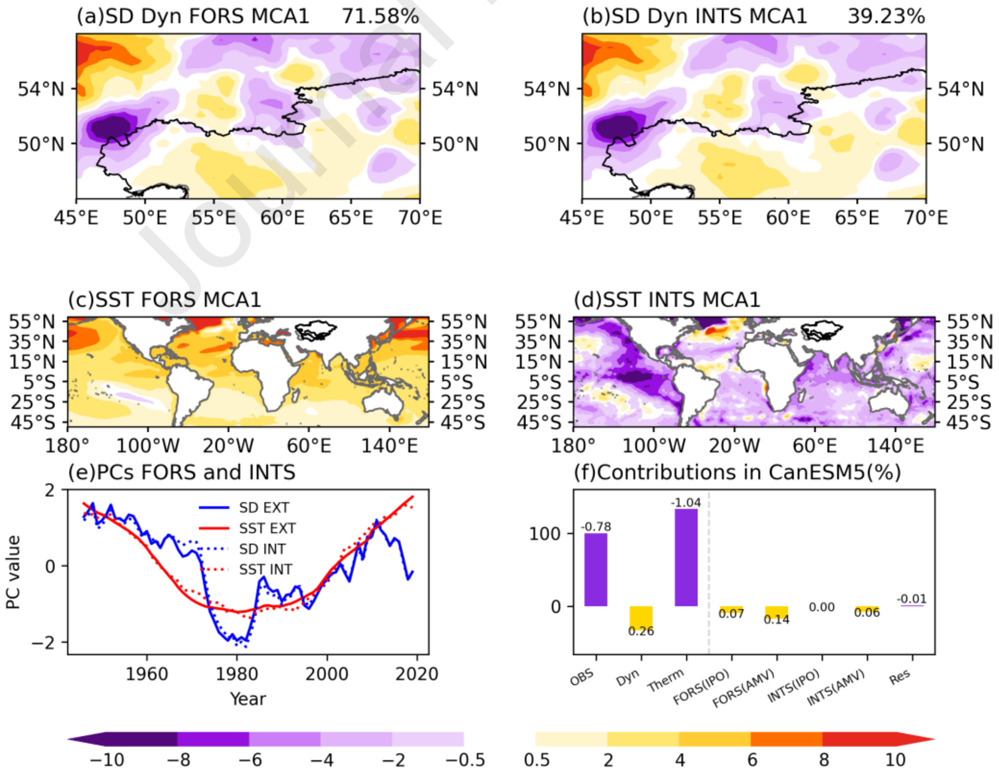

Fig. 4. (a, c) Spatial patterns of MCA1 between dynamically induced SD in observations and externally forced detrended global SST anomalies from CanESM5 during 1941–2024 (The values in the upper-right corner indicate the variance explained by MCA1), (b, d) same as (a, c), but for internally generated SST

anomalies, (e) normalized PC1 time series of dynamically induced SD (blue) and externally forced SST (red) (The dashed line denotes the corresponding PC1 associated with internally generated SST variability) and (f) contributions of trends of SD-related components (Numbers on the bars indicate the areal-mean SD trends over northwest CA).

Given that dynamical SD variability is primarily regulated by local atmospheric circulation variability and large-scale teleconnections in which SST acts as a key driver, we further quantify the relative contributions of IPO and AMV to the observed dynamical SD trend during the focused present period (1979–2024). The contributions are estimated by weighting IPO- and AMV-related SD trends by their respective MCA explained covariance fractions and normalizing them by the corresponding dynamical SD PC1 trend, rather than solely from regression coefficients. Taking both regression sensitivity and the IPO and AMV trends into account targets their contributions to the SD trend itself rather than to the interdecadal amplitude of SST signals. In CanESM5, externally forced SST variability accounts for 82% of the observed dynamical SD trend during the present period, with externally forced IPO and AMV phase transitions contributing 0.06 and 0.11 mm per year, respectively, while internally generated SST variability contributes only 0.05 mm per year, primarily through AMV-related variability. The residual term, representing local atmospheric internal variability and teleconnections not captured by IPO or AMV, accounts for a negligible −5% contribution (Fig. 4f). Consistent results are obtained from the low-ECS MIROC6 model, in which externally forced IPO and AMV contribute 0.05 and 0.12 mm per year, respectively, while internal SST variability and residual atmospheric variability account for 14% and 5% of the dynamical SD trend (Fig. A6f). These results support that anthropogenically forced interdecadal SST variability plays a dominant and irreplaceable role in shaping present-day dynamical SD trends over northwest CA. Although internally generated SST variability continues to modulate SD variability, its magnitude is insufficient to offset or overturn the externally forced responses.

A detailed decomposition of SD trends not only clarifies the contributions of various physical processes to winter snow dynamic accumulation but also provides valuable insights into the lagged impacts on spring hydroclimate over northwest CA. Dynamical adjustment is further applied to precipitation and T2m in the subsequent spring. The regressions of the total, dynamically driven, and thermodynamically driven components of precipitation and T2m with their preceding winter SD counterparts are shown in Fig. 5. Prior to regression, interdecadal variability is removed using an 11-year running mean to isolate the variability linkage between winter SD and subsequent spring climate, thereby minimizing spurious thermodynamic causality arising from long-term global warming. For spring precipitation, the grid-to-grid regression with total winter SD is predominantly positive over central and southwestern northwest CA, although some regions do not reach statistical significance, reflecting the dominant influences of dynamical processes (Fig. 5a, c, e). Specifically, the dynamically driven components of both winter SD and spring precipitation exhibit a positive relationship over northern and central northwest CA (Fig. 5c), indicating that circulation anomalies favorable for enhanced winter snow accumulation may also promote moisture convergence and precipitation in the subsequent spring. In contrast, the thermodynamically driven components show a widespread but weak negative correlation (Fig. 5e). On the one hand, a spatially homogeneous and statistically significant surface cooling in spring across northwest CA is almost entirely governed by thermodynamical processes linked to reduced winter SD (Fig. 5b, f), whereas the dynamically driven contribution is negligible in the regional mean (Fig. 5d). Physically, reduced winter SD decreases near-surface atmospheric moisture content, leading to a reduction in downward longwave radiative feedback to the surface (Fig. 5f). The resulting near-surface cooling weakens the vertical temperature gradient between the surface and the lower atmosphere, enhances static stability, and suppresses turbulent heat exchange. The combined reduction in downward longwave radiation and sensible heat flux decreases the net energy input into the surface boundary-layer system, reinforcing near-surface cooling and ultimately manifesting as colder spring T2m (Fig. 5f).

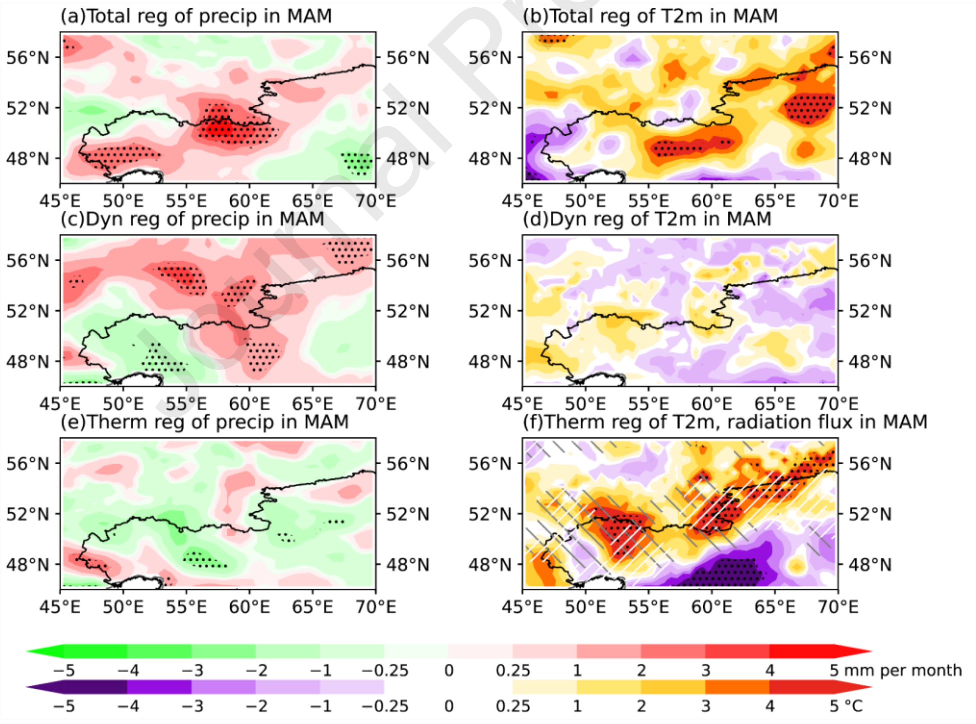

Fig. 5. (a, b) Regression patterns of total precipitation and T2m in March–May (MAM) with preceding winter total SD, and (c–f) same as (a, b), but for the dynamical and thermodynamical components of precipitation, T2m, and SD, respectively (In (f), gray and white hatched areas represent increased downward longwave radiation and sensible heat flux, respectively, exceeding 0.8 W/m^2. Stippled areas indicate regression coefficients significant at the 90% confidence level).

4. Conclusions and discussion

This study investigates the physical mechanisms driving the observed SD decline in northwest CA over the period 1979–2024, with a focus on quantifying the relative contributions of atmospheric dynamics and thermodynamic warming. The results demonstrate that the observed shallowing trend in SD is primarily driven by thermodynamic processes associated with anthropogenic warming, accounting for approximately −1.00 mm per year of the total decline in the present climate, and closely reproducing the observed spatial pattern. This forced response is robust across large-ensemble simulations from both high- and low-ECS models and is projected to accelerate under the SSP5-8.5 scenario. In contrast, atmospheric dynamical processes partially offset the thermodynamically driven SD decline in the present climate, contributing a positive trend of approximately 0.22 mm per year through enhanced northerly and easterly anomalies over northwest CA, which favor cold-air advection and locally enhanced snow accumulation.

At interdecadal timescales, dynamically induced SD accumulations in observations are modulated by large-scale atmospheric teleconnections associated with SST variability in the tropical eastern Pacific and North Atlantic, represented by the IPO and AMV. Cooling in the tropical eastern Pacific and simultaneous North Atlantic warming excites an eastward-propagating Rossby wave train, leading to anomalous high pressure over western Siberia and a low-pressure response over central-eastern CA. This pattern strengthens cold advection into northwest CA and favors snow accumulation. Quantitative attribution based on large-ensemble models reveals that externally forced SST changes dominate this dynamical pathway, explaining about 82% of the dynamically driven SD trend in CanESM5 during 1979–2024, while internal SST variability and local atmospheric circulation contribute a smaller yet non-negligible fraction (~23%) and −5%, respectively. The dominant role of externally forced SST-driven teleconnections is also supported by the low-ECS MIROC6 model.

Beyond winter snow processes, SD exerts a lagged influence on subsequent spring climate conditions in northwest CA through snow hydrological effect and surface energy balance. Winter SD modulates spring precipitation, primarily via dynamical processes involving circulation-driven moisture transport. In contrast, the positive linkage between winter SD and spring T2m is overwhelmingly thermodynamic. Reduced winter SD limits near-surface moisture availability and weakens the temperature gradient between the surface and the lower atmosphere, leading to reduced downward longwave radiative feedback and sensible heat exchange, accelerating spring cooling. These results establish winter SD as a physically grounded precursor for spring hydroclimatic variability in CA.

The findings suggest important implications for understanding how global warming may alter regional climate, potentially causing precipitation and surface temperature shifts. As long-term warming accelerates the transformation of the regional hydrological cycle in CA, rainfall–snowfall interactions are expected to become increasingly complex, with direct consequences for runoff and water resource replenishment (Chevallier et al., 2014; Li et al., 2019; Li et al., 2020b). Therefore, sustained monitoring of winter SST anomalies in the equatorial Pacific and North Atlantic is essential for diagnosing circulation-driven SD variability, as ocean-forced teleconnections can partially offset SD shallowing dominated by anthropogenic warming. At the same time, SD itself acts as an important precursor signal that winter SD anomalies exert lagged influences on spring climate by modulating precipitation through both dynamical and thermodynamical pathways and by controlling near-surface air temperature via snow–albedo feedback, thereby affecting snowmelt-driven river discharge during the growing season. Joint monitoring of SST variability and winter SD therefore provides valuable early indicators for spring planting and irrigation planning in CA. It should also be noted that other lower-boundary forcings, such as Barents Sea ice variability, may also modulate CA circulation and warrant dedicated investigation (Chen et al., 2022; Yao et al., 2024a). Finally, advancing the quality and consistency of snow-related climate datasets through the integration and continuous refinement of ground-based observations and satellite-derived products is critical to strengthening climate understanding and enabling more robust climate impact assessments, with direct relevance for water resource management, agricultural planning, and sustainable development in this climate-sensitive but data-sparse region.

Declaration of competing interests

The authors declare no conflict of interest.

CRediT authorship contribution statement

Meng-Yuan Yao: Writing — review & editing, Writing — original draft, Visualization, Validation, Methodology, Investigation, Formal analysis, Data curation, Conceptualization. **Hao-Su Tang**: Writing — review & editing, Supervision, Investigation, Conceptualization. **Gang Huang**: Supervision, Resources, Funding acquisition.

Acknowledgments

This work was supported by the National Natural Science Foundation of China (42530606, 42261144687) and the National Key R&D Program of China (2025YFF0812000). We acknowledge the two anonymous reviewers for their careful reviews and valuable suggestions, which greatly strengthened this manuscript.

References

Barnett, T.P., Adam, J.C., Lettenmaier, D.P., 2005. Potential impacts of a warming climate on water availability in snow-dominated regions. Nature 438(7066), 303–309. https://doi.org/10.1038/nature04141.

Chen, H., Sun, J., Lin, W., 2020. Anthropogenic influence would increase intense snowfall events over parts of the Northern Hemisphere in the future. Environ. Res. Lett. 15(11), 114022. https://doi.org/10.1088/1748-9326/abbc93.

Chen, P., Yao, J., Mao, W., 2023. Interannual snowfall variations in Central Asia and their association with ENSO and stratospheric polar vortex during winter. Clim. Dyn. 61(3), 1505–1517. https://doi.org/10.1007/s00382-022-06639-w.

Chen, X., Jia, X., Wu, R., et al., 2022. Interannual variation and prediction of wintertime precipitation in Central Asia. J. Clim. 35(14), 4771–4789. https://doi.org/10.1175/JCLI-D-21-0951.1.

Chen, Y., Li, W., Deng, H., et al., 2016. Changes in Central Asia's water tower: past, present and future. Sci. Rep. 6(1), 35458

Chevallier, P., Pouyaud, B., Mojaïsky, M., et al., 2014. River flow regime and snow cover of the Pamir Alay (Central Asia) in a changing climate. Hydrol. Sci. J. 59, 1491–1506. https://doi.org/10.1080/02626667.2013.838004.

Dai, A., Fyfe, J.C., Xie, S., et al., 2015. Decadal modulation of global surface temperature by internal climate variability. Nat. Clim. Change 5(6), 555–559. https://doi.org/10.1038/nclimate2605.

Deser, C., Phillips, A., Bourdette, V., et al., 2012. Uncertainty in climate change projections: the role of internal variability. Clim. Dyn. 38(3), 527–546. https://doi.org/10.1007/s00382-010-0977-x.

Deser, C., Terray, L., Phillips, A.S., 2016. Forced and internal components of winter air temperature trends over North America during the past 50 years: mechanisms and implications. J. Clim. 29(6), 2237–2258. https://doi.org/10.1175/JCLI-D-15-0304.1.

Dietz, A.J., Conrad, C., Kuenzer, C., et al. 2014. Identifying changing snow cover characteristics in Central Asia between 1986 and 2014 from remote sensing data. Remote Sens. 6(12), 12752–12775. https://doi.org/10.3390/rs61212752.

FAO (Food and Agriculture Organization of the United Nations), 2001. Foodcrops & Shortages No.4. https://www.fao.org/4/Y1913E/pays/asia0109.htm.

Gelaro, R., McCarty, W., Suárez, M.J., et al., 2017. The Modern-era retrospective analysis for research and applications, version 2 (MERRA-2). J. Clim. 30(14), 5419–5454. https://doi.org/10.1175/JCLI-D-16-0758.1.

Gottlieb, A.R., Mankin, J.S., 2024. Evidence of human influence on Northern Hemisphere snow loss. Nature 625(7994), 293–300. https://doi.org/10.1038/s41586-023-06794-y.

Han, T., He, S., Hao, X., et al., 2018. Recent interdecadal shift in the relationship between northeast China's winter precipitation and the North Atlantic and Indian Oceans. Clim. Dyn. 50(3), 1413–1424. https://doi.org/10.1007/s00382-017-3694-x.

Harris, I., Osborn, T.J., Jones, P., et al., 2020. Version 4 of the CRU TS monthly high-resolution gridded multivariate climate dataset. Sci. Data 7(1), 109. https://doi.org/10.1038/s41597-020-0453-3.

Held, I.M., Soden, B.J., 2006. Robust responses of the hydrological cycle to global warming. J. Clim. 19(21), 5686–5699. https://doi.org/10.1175/JCLI3990.1.

Hersbach, H., Bell, B., Berrisford, P., et al., 2020. The ERA5 global reanalysis. Q. J. R. Meteorol. Soc. 146(730), 1999–2049. https://doi.org/10.1002/qj.3803.

Hoelzle, M., Azisov, E., Barandun, M., et al., 2017. Re-establishing glacier monitoring in Kyrgyzstan and Uzbekistan, Central Asia. Geosci. Instrum. Method. Data Syst. 6(2), 397–418. https://doi.org/10.5194/gi-6-397-2017.

Jiang, J., Zhou, T., Chen, X., et al., 2021. Central Asian precipitation shaped by the tropical Pacific decadal variability and the Atlantic multidecadal variability. J. Clim. 34(18), 7541–7553. https://doi.org/10.1175/jcli-d-20-0905.1.

Jiang, Y., Che, T., Dai, L., 2025. Inconsistent response patterns of snow cover duration and snow depth over the Tibetan Plateau to global warming. Adv. Clim. Change Res. 16(3), 501–511. https://doi.org/https://doi.org/10.1016/j.accre.2025.03.007.

Kosaka, Y., Kobayashi, S., Harada, Y., et al., 2024. The JRA–3Q reanalysis. J. Meteorol. Soc. Jpn. Ser. II 102(1), 49–109. https://doi.org/10.2151/jmsj.2024-004.

Koster, R.D., Mahanama, S.P.P., Livneh, B., et al., 2010. Skill in streamflow forecasts derived from large-scale estimates of soil moisture and snow. Nat. Geosci. 3(9), 613–616. https://doi.org/10.1038/ngeo944.

Li, Y., Gong, H., Chen, W., et al., 2024. Attribution of drought trends on the Mongolian Plateau over the past decades. Environ. Res. Lett. 19(7), 074034. https://doi.org/10.1088/1748-9326/ad560d.

Li, Y., Tao, H., Su, B., et al., 2019. Impacts of 1.5 °C and 2 °C global warming on winter snow depth in Central Asia. Sci. Total Environ. 651, 2866–2873. https://doi.org/10.1016/j.scitotenv.2018.10.126.

Li, Z., Chen, Y., Li, Y., et al., 2020a. Declining snowfall fraction in the alpine regions, Central Asia. Sci. Rep. 10(1), 3476. https://doi.org/10.1038/s41598-020-60303-z.

Li, Z., Fang, G., Chen, Y., et al., 2020b. Agricultural water demands in Central Asia under 1.5 °C and 2.0 °C global warming. Agric. Water Manag. 231, 106020. https://doi.org/10.1016/j.agwat.2020.106020.

Lin, W., Chen, H., Wang, W., et al., 2024. Anthropogenic influence has significantly affected snowfall changes in Eurasia. Atmos. Res. 297, 107125. https://doi.org/10.1016/j.atmosres.2023.107125.

Liu, Y., Cai, W., Zhang, Y., et al., 2024. Near-term projection of Amazon rainfall dominated by phase transition of the Interdecadal Pacific Oscillation. npj Clim. Atmos. Sci. 7(1), 46. https://doi.org/10.1038/s41612-024-00587-4.

Ma, L., Wei, Z., Ding, R., et al., 2025. Interannual responses of Arctic temperatures to Eurasian snow cover variations in early spring. Atmos. Res. 315, 107866. https://doi.org/10.1016/j.atmosres.2024.107866.

Man, K., Luterbacher, J., Holland, D.M., et al., 2025. Century-long West Antarctic snow accumulation changes induced by tropical teleconnections. Sci. Adv. 11(5), eadr2821. https://doi.org/10.1126/sciadv.adr2821.

Menne, M.J., Durre, I., Vose, R.S., et al., 2012. An overview of the global historical climatology network-daily database. J. Atmos. Oceanic Technol. 29(7), 897–910. https://doi.org/10.1175/JTECH-D-11-00103.1.

Oki, T., Kanae, S., 2006. Global hydrological cycles and world water resources. Science 313(5790), 1068–1072. https://doi.org/10.1126/science.1128845.

Pyper, B., Peterman, R.M., 1998. Comparison of methods to account for autocorrelation in correlation analyses of fish data. Can. J. Fish. Aquat. Sci. 55, 2127–2140. https://doi.org/10.1139/f98-104.

Qin, M., Dai, A., Hua, W., 2020. Quantifying contributions of internal variability and external forcing to Atlantic multidecadal variability since 1870. Geophys. Res. Lett. 47(22), e2020GL089504. https://doi.org/10.1029/2020GL089504.

Rayner, N., Parker, D.E., Horton, E., et al., 2003. Global analyses of sea surface temperature, sea ice, and night marine air temperature since the late nineteenth century. J. Geophys. Res. Atmos. 108(D14), 4407. https://doi.org/10.1029/2002JD002670.

Rodell, M., Houser, P.R., Jambor, U., et al., 2004. The global land data assimilation system. Bull. Am. Meteorol. Soc. 85(3), 381–394. https://doi.org/10.1175/BAMS-85-3-381.

Schmale, J., Flanner, M., Kang, S., et al., 2017. Modulation of snow reflectance and snowmelt from Central Asian glaciers by anthropogenic black carbon. Sci. Rep. 7(1), 40501. https://doi.org/10.1038/srep40501.

Sun, Y., Chen, H., Zhu, S., et al., 2021. Influence of the Eurasian spring snowmelt on summer land surface warming over northeast Asia and its associated mechanism. J. Clim. 34(12), 4851–4869. https://doi.org/10.1175/JCLI-D-20-0756.1.

Swart, N.C., Cole, J.N.S., Kharin, V.V., et al., 2019. The Canadian Earth System Model version 5 (CanESM5.0.3). Geosci. Model Dev. 12(11), 4823–4873. https://doi.org/10.5194/gmd-12-4823-2019.

Takaya, K., Nakamura, H., 2001. A formulation of a phase-independent wave-activity flux for stationary and migratory quasigeostrophic eddies on a zonally varying basic flow. J. Atmos. Sci. 58, 608–627. https://doi.org/10.1175/1520-0469(2001)058<0608:AFOAPI>2.0.CO;2.

Tatebe, H., Ogura, T., Nitta, T., et al., 2019. Description and basic evaluation of simulated mean state, internal variability, and climate sensitivity in MIROC6. Geosci. Model Dev. 12(7), 2727–2765. https://doi.org/10.5194/gmd-12-2727-2019.

Wang, L., Fan, K., Xu, Z., 2020. Comparison of the causes of high-frequency heavy and light snowfall on interannual timescales over northeast China. Atmosphere 11(9), 936 (Chinese).

Wu, M., Zhou, T., Li, C., et al., 2021. A very likely weakening of Pacific Walker Circulation in constrained near-future projections. Nat. Commun. 12(1), 6502. https://doi.org/10.1038/s41467-021-26693-y.

Wu, R., Liu, G., Zhao, P., 2014. Contrasting Eurasian spring and summer climate anomalies associated with western and eastern Eurasian spring snow cover changes. J. Geophys. Res. Atmos. 119. https://doi.org/10.1002/2014JD021764.

Yao, M., Li, J., Zheng, C., et al., 2024a. How predictable is the anomaly pattern of summer extreme high-temperature days over Central Asia? Clim. Dyn. 62(8), 7651–7664. https://doi.org/10.1007/s00382-024-07299-8.

Yao, M., Tang, H., Huang, G., 2024b. Inter-model uncertainty in projecting precipitation changes over Central Asia under global warming. Geophys. Res. Lett. 51(24), e2024GL111989. https://doi.org/10.1029/2024GL111989.

Yao, M., Tang, H., Huang, G., 2025. Roles of external forcing and internal variability in winter precipitation changes over Central Asia. Earths Future 13(7), e2025EF006064. https://doi.org/10.1029/2025EF006064.

Yao, T., Xue, Y., Chen, D., et al., 2019. Recent third pole’s rapid warming accompanies cryospheric melt and water cycle intensification and interactions between monsoon and environment: multidisciplinary approach with observations, modeling, and analysis. Bull. Am. Meteorol. Soc. 100(3), 423–444. https://doi.org/10.1175/BAMS-D-17-0057.1.

Yao, Y., Luo, Y., Huang, J., et al., 2021. Improving the downscaled springtime temperature in Central Asia through assimilating meteorological and snow cover observations. Atmos. Res. 258, 105619. https://doi.org/10.1016/j.atmosres.2021.105619.

Zelinka, M.D., Myers, T.A., McCoy, D.T., et al., 2020. Causes of higher climate sensitivity in CMIP6 models. Geophys. Res. Lett. 47(1), e2019GL085782. https://doi.org/10.1029/2019GL085782.

Zhang, J., Chen, Z., Chen, H., et al., 2020. North Atlantic multidecadal variability enhancing decadal extratropical extremes in boreal late summer in the early twenty-first century. J. Clim. 33(14), 6047–6064. https://doi.org/10.1175/JCLI-D-19-0536.1.

Zhang, Y., Kang, S., Gao, T., et al., 2019. Dissolved organic carbon in snow cover of the Chinese Altai Mountains, Central Asia: concentrations, sources and light-absorption properties. Sci. Total Environ. 647, 1385–1397. https://doi.org/10.1016/j.scitotenv.2018.07.417.

Zhou, H., Aizen, E., Aizen, V., 2017. Seasonal snow cover regime and historical change in Central Asia from 1986 to 2008. Global Planet. Change 148, 192–216. https://doi.org/10.1016/j.gloplacha.2016.11.011.

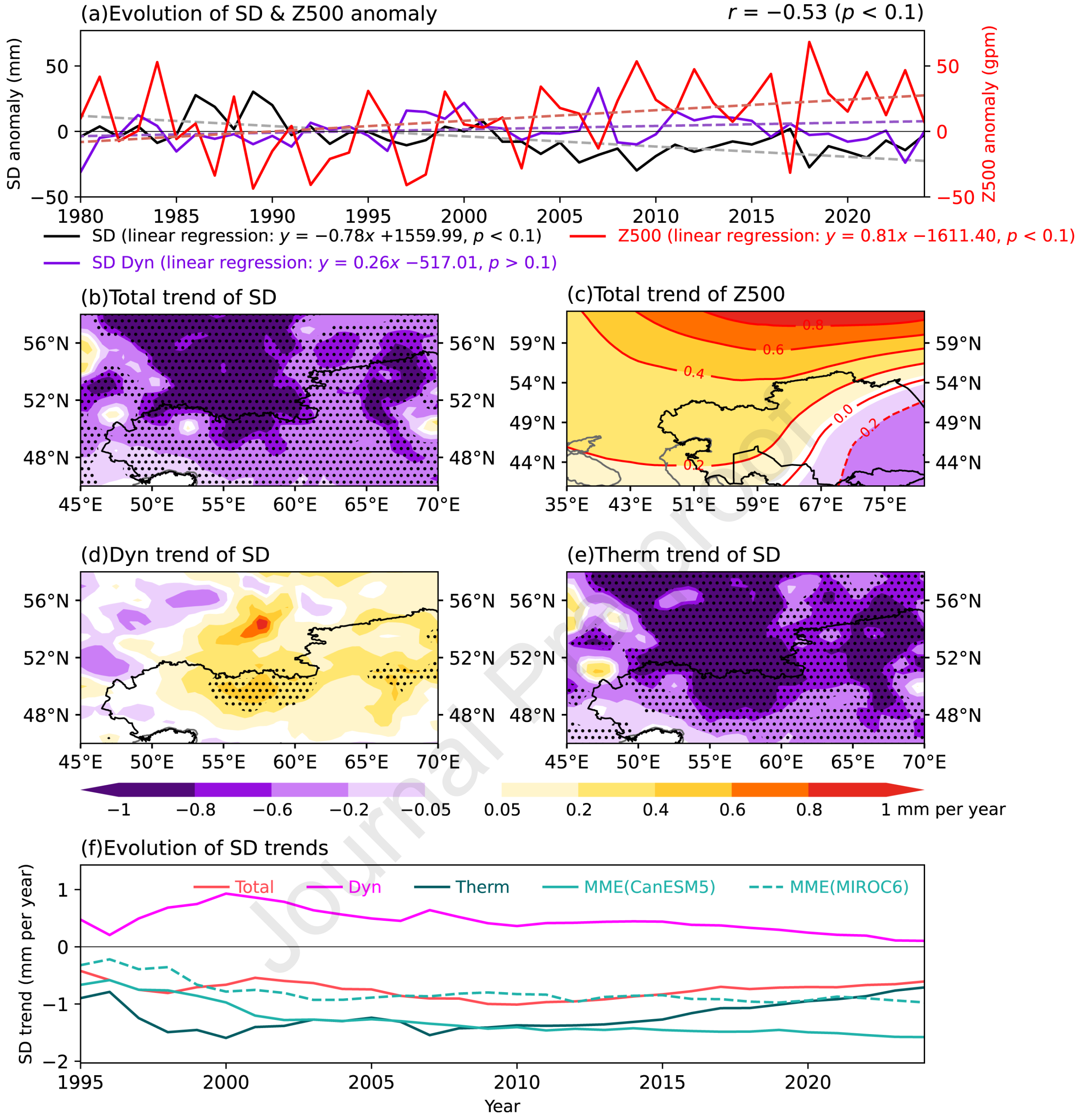
(a)Evolution of SD & Z500 anomaly
r = −0.53 (p < 0.1)
SD anomaly (mm)
Z500 anomaly (gpm)
50
0
−50
1980
1985
1990
1995
2000
2005
2010
2015
2020
SD (linear regression: y = −0.78x +1559.99, p < 0.1)
Z500 (linear regression: y = 0.81x −1611.40, p < 0.1)
SD Dyn (linear regression: y = 0.26x −517.01, p > 0.1)
(b)Total trend of SD
(c)Total trend of Z500
56°N
52°N
48°N
45°E
50°E
55°E
60°E
65°E
70°E
59°N
54°N
49°N
44°N
35°E
43°E
51°E
59°E
67°E
75°E
0.8
0.6
0.4
0.2
0.0
-0.2
(d)Dyn trend of SD
(e)Therm trend of SD
−1
−0.8
−0.6
−0.2
−0.05
0.05
0.2
0.4
0.6
0.8
1 mm per year
(f)Evolution of SD trends
Total
Dyn
Therm
MME(CanESM5)
MME(MIROC6)
SD trend (mm per year)
1
0
−1
−2
1995
2000
2005
2010
2015
2020
Year

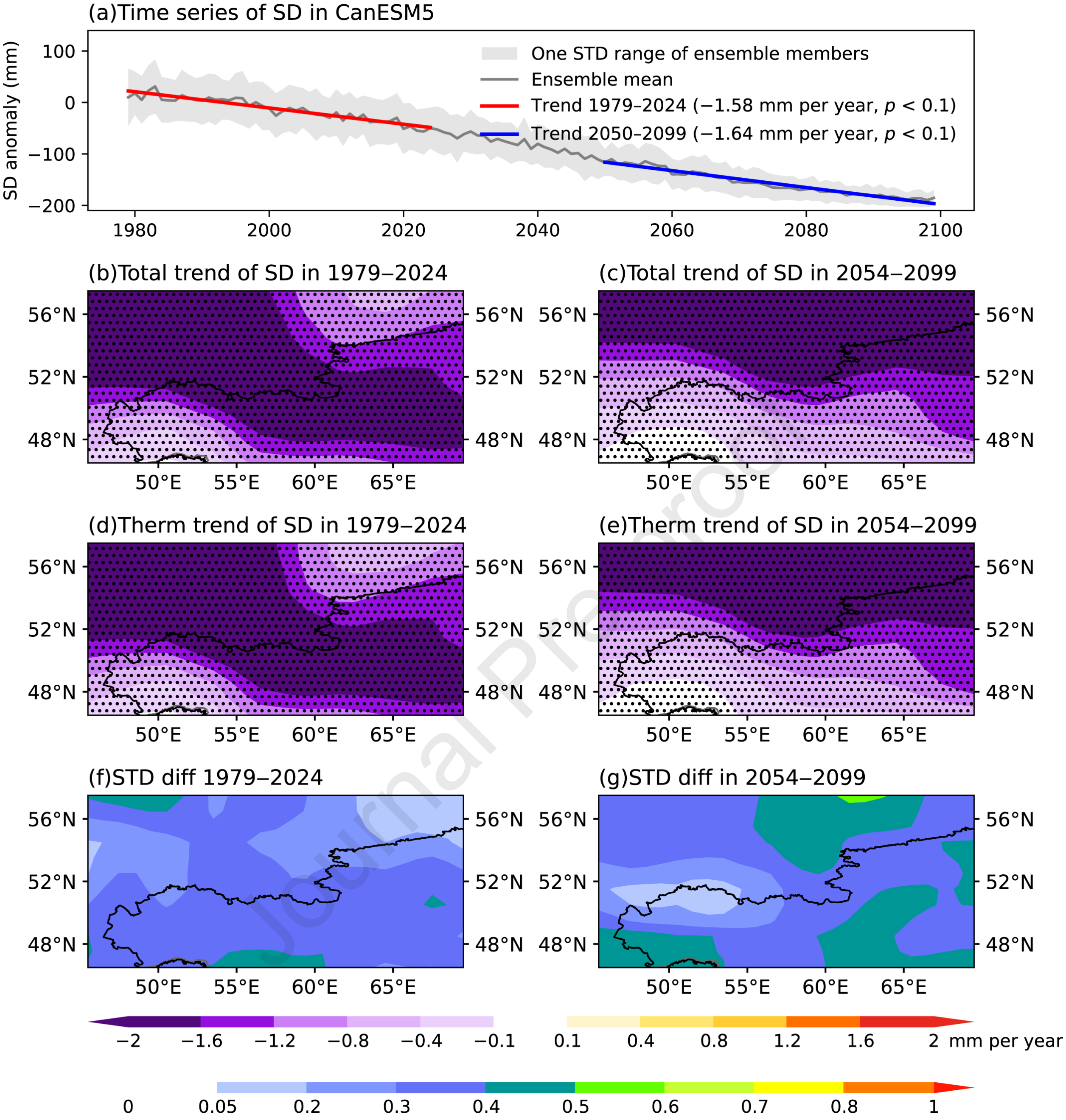
(a)Time series of SD in CanESM5
SD anomaly (mm)
100
0
−100
−200
1980
2000
2020
2040
2060
2080
2100
One STD range of ensemble members
Ensemble mean
Trend 1979–2024 (−1.58 mm per year, $p < 0.1$)
Trend 2050–2099 (−1.64 mm per year, $p < 0.1$)
(b)Total trend of SD in 1979–2024
(c)Total trend of SD in 2054–2099
(d)Therm trend of SD in 1979–2024
(e)Therm trend of SD in 2054–2099
(f)STD diff 1979–2024
(g)STD diff in 2054–2099
56°N
52°N
48°N
50°E
55°E
60°E
65°E
−2
−1.6
−1.2
−0.8
−0.4
−0.1
0.1
0.4
0.8
1.2
1.6
2
mm per year
0
0.05
0.2
0.3
0.4
0.5
0.6
0.7
0.8
1

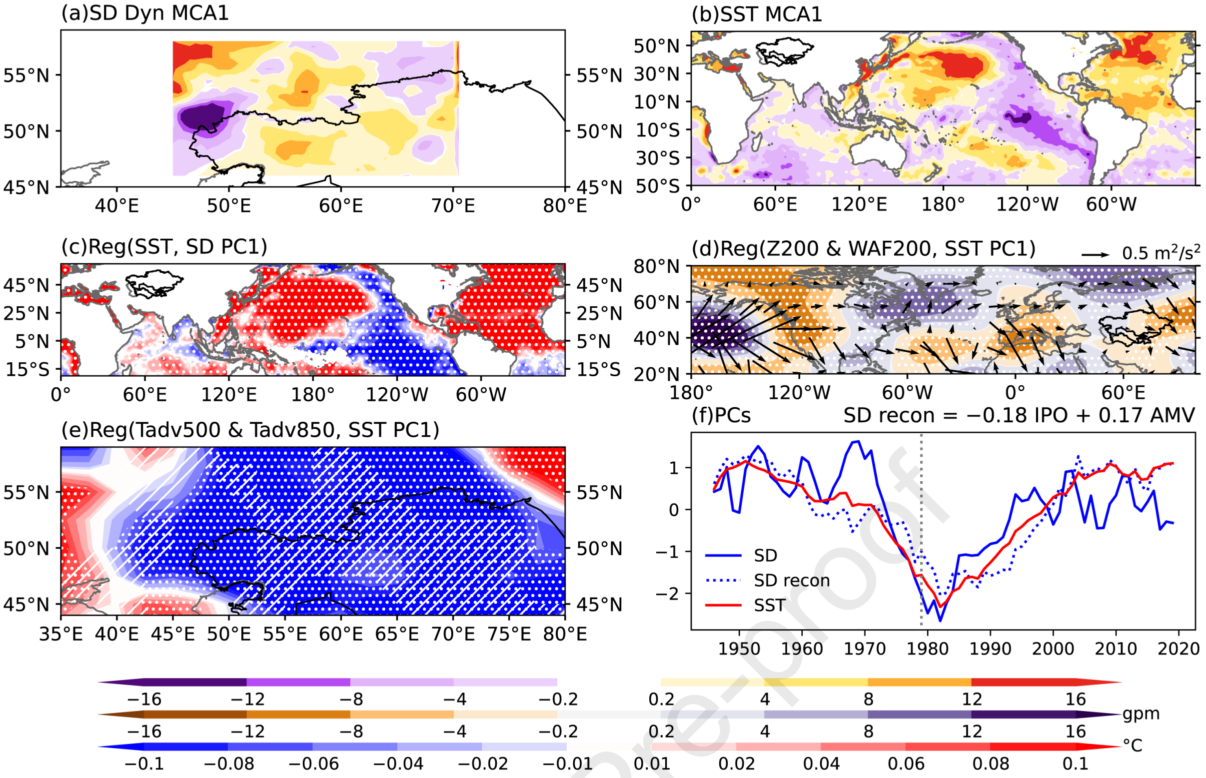
(a)SD Dyn MCA1
55°N
50°N
45°N
40°E
50°E
60°E
70°E
80°E
(b)SST MCA1
50°N
30°N
10°N
10°S
30°S
50°S
0°
60°E
120°E
180°
120°W
60°W
(c)Reg(SST, SD PC1)
45°N
25°N
5°N
15°S
0°
60°E
120°E
180°
120°W
60°W
(d)Reg(Z200 & WAF200, SST PC1)
0.5 m²/s²
80°N
60°N
40°N
20°N
180°
120°W
60°W
0°
60°E
(e)Reg(Tadv500 & Tadv850, SST PC1)
55°N
50°N
45°N
35°E
40°E
45°E
50°E
55°E
60°E
65°E
70°E
75°E
80°E
(f)PCs
SD recon = −0.18 IPO + 0.17 AMV
1
0
−1
−2
SD
SD recon
SST
1950
1960
1970
1980
1990
2000
2010
2020
−16
−12
−8
−4
−0.2
0.2
4
8
12
16
gpm
−16
−12
−8
−4
−0.2
0.2
4
8
12
16
°C
−0.1
−0.08
−0.06
−0.04
−0.02
−0.01
0.01
0.02
0.04
0.06
0.08
0.1

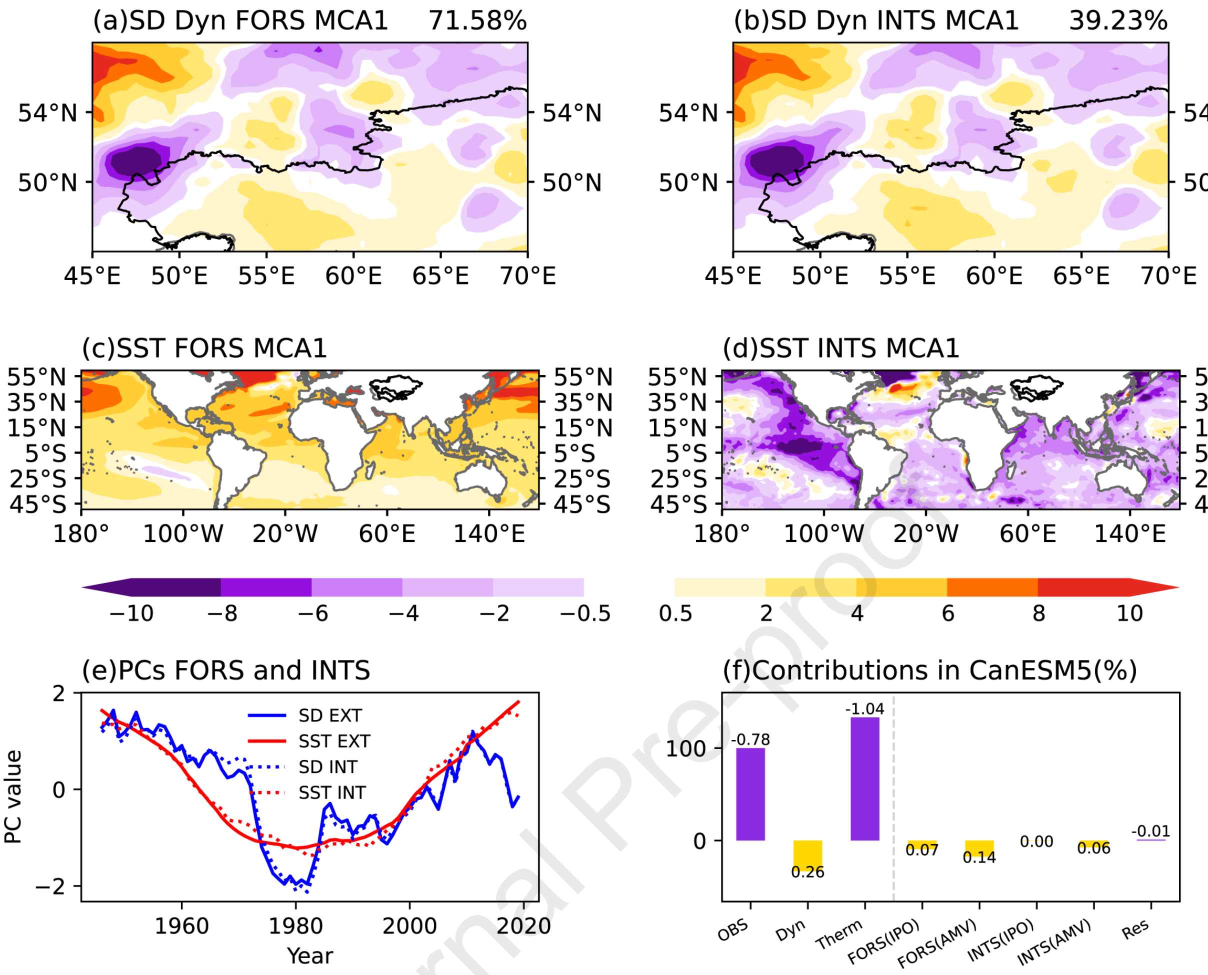
(a)SD Dyn FORS MCA1 71.58%
(b)SD Dyn INTS MCA1 39.23%
54°N
50°N
45°E
50°E
55°E
60°E
65°E
70°E
(c)SST FORS MCA1
(d)SST INTS MCA1
55°N
35°N
15°N
5°S
25°S
45°S
180°
100°W
20°W
60°E
140°E
−10
−8
−6
−4
−2
−0.5
0.5
2
4
6
8
10
(e)PCs FORS and INTS
SD EXT
SST EXT
SD INT
SST INT
PC value
2
0
−2
1960
1980
2000
2020
Year
(f)Contributions in CanESM5(%)
100
0
-0.78
0.26
-1.04
0.07
0.14
0.00
0.06
-0.01
OBS
Dyn
Therm
FORS(IPO)
FORS(AMV)
INTS(IPO)
INTS(AMV)
Res

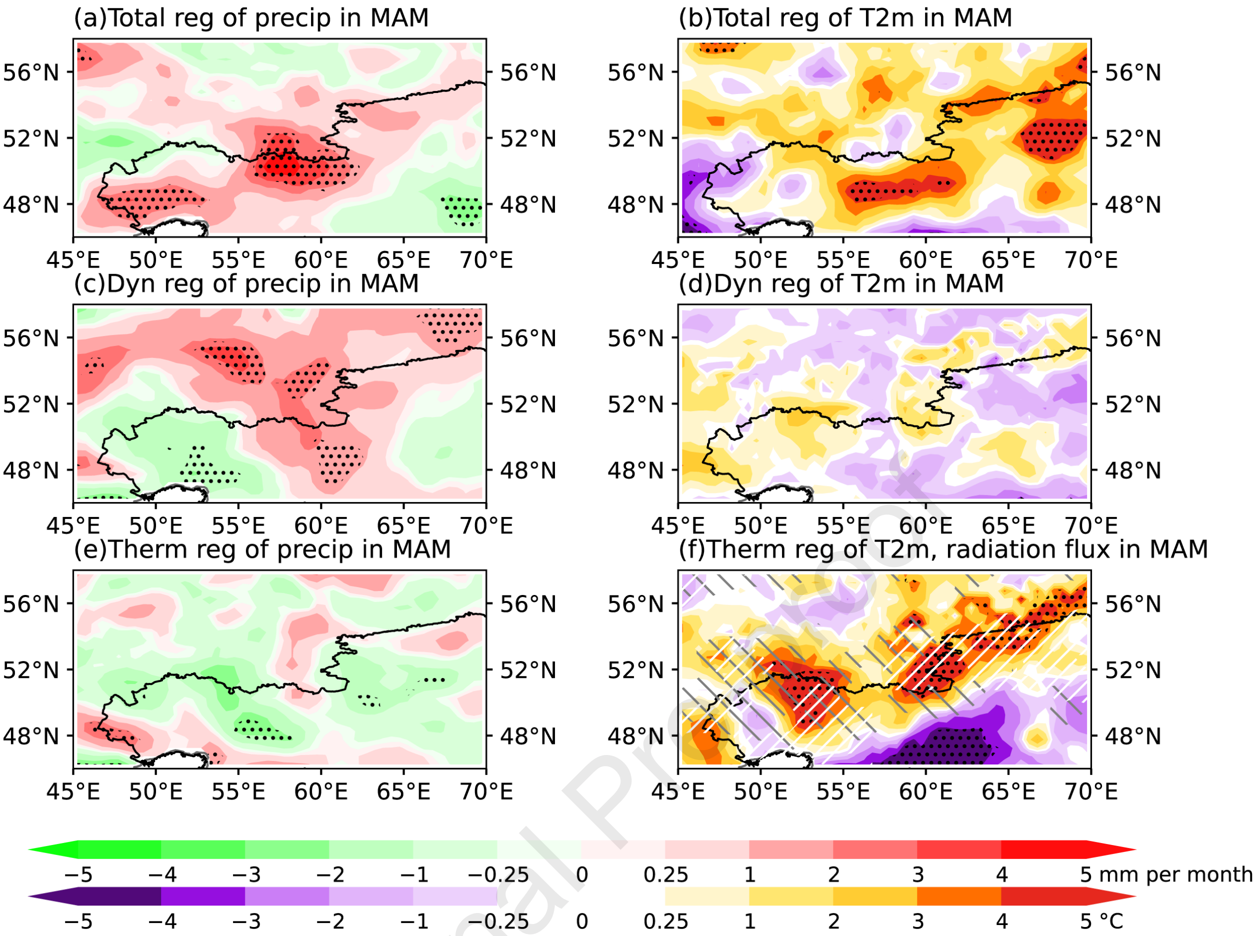
(a)Total reg of precip in MAM
(b)Total reg of T2m in MAM
(c)Dyn reg of precip in MAM
(d)Dyn reg of T2m in MAM
(e)Therm reg of precip in MAM
(f)Therm reg of T2m, radiation flux in MAM
56°N
52°N
48°N
45°E
50°E
55°E
60°E
65°E
70°E
−5
−4
−3
−2
−1
−0.25
0
0.25
1
2
3
4
5 mm per month
5 °C

Declaration of competing interest

The authors declare no conflict of interest.